Multi-view 3D InISAR Imaging

F. Salvetti, M. Martorella, E. Giusti and D. Staglianò

***Abstract*—Three-dimensional (3D) ISAR imaging has been proven feasible by combining traditional ISAR imaging and interferometry. Such technique, namely Inteferometric ISAR (InISAR), allows for the main target scattering centres to be mapped into a 3D spatial domain, therefore forming 3D images under the form of 3D point clouds. 3D InISAR overcomes some main limitations of traditional 2D ISAR imaging, such as the problem of cross-range scaling and unknown image projection plane (IPP). Despite the great advantage of 3D imaging over traditional 2D imaging, some issues remain, such as scatterer scintillation, shadowing effects, poor SNR, etc., which limit the effectiveness of 3D imaging. A solution to these issues can be found in the use of multiple 3D views, which can be obtained exploiting either multi-temporal or multi-perspective configurations or a combination of both. This paper propose this concept and develops the image fusion algorithms that are necessary to produce multi-view 3D ISAR images. The effectiveness of the proposed technique is tested by using real data collected with a multi-static InISAR system.**

***Index Terms*—Inverse Synthetic Aperture Radar (ISAR), 3D Radar Imaging, Radar Interferometry, 3D incoherent imge fusion, Multi-view Radar Imaging.**

I. Introduction

THree dimensional interferometic ISAR (InISAR) algorithms [1]–[6] have been proposed recently as a means to obtain 3D point clouds that represent the target. The recently proposed 3D InISAR technique overcomes the limitations of standard 2D ISAR techniques. 2D ISAR techniques generate a 2D image of the target, which represents a 2D projection of the true three-dimensional target reflectivity onto an image plane. The orientation of the image plane strongly depends on the radar-target geometry and on the target motions, which are typically unknown. The result is that the target projection onto the image plane cannot be predicted and the interpretation of the resulting ISAR images becomes complicated. Under these conditions, the projected two-dimensional image can only provide limited information and is often not sufficient for identifying and recognizing the target. To solve this problem, the idea is to form a 3D reconstruction of the target as to completely avoid the problems related to the orientation of the imaging plane and the consequent misinterpretation of the 2D ISAR image.

Monostatic 3D InISAR suffers, however, of some critical issues. Among others, target scintillation, geometrically adverse cases, such as that represented by a target that deliberately advances along the radar Line of Sight (LoS), producing ISAR images with no Doppler extension and shadowing effects.

F. Salvetti, M. Martorella, E. Giusti and D. Staglianò are with the Department of Information Engineering, University of Pisa, Pisa, 56122 Italy and the National Laboratory of Radar and Surveillance Systems (RaSS) - CNIT, Pisa, 56124 Italy, e-mail: {federica.salvetti, elisa.giusti}@cnit.it {marco.martorella}@iet.unipi.it {daniele.stagliano}@for.unipi.it.

The first may be overcome by observing the target for a sufficiently long time to form a number of 3D reconstructions. Such a collection of 3D reconstructions may be then jointly used to obtain a fused 3D reconstruction. Multi-temporal 3D reconstruction may however not solve the problem of shadowing since the target may show the same side to the radar for all the available observation time. Then, a possible solution for both the shadowing and geometrically adverse cases, comes from the use of multistatic InISAR system where multiple 3D reconstructions can be obtained from quite different aspect angles.

Both solutions necessitate however to combine data relative to different acquisition times or different sensors.

Some papers have been proposed in the recent literature that address the problem of how to combine data of a net of distributed radars [7]–[9]. Fusion may be implemented either at raw-data level or at image level. The first however requires a high degree of coherence (both in frequency and in phase) which may be difficult to reach in a net of spatially distributed radars.

In this paper the algorithm proposed in [7] is adapted to handle both multi-temporal and multi-perspective configurations and is then tested by using real data acquired during the SET-196 NATO Trials, which took place in Livorno (Italy) in September-October 2014. The radar network was composed of three InISAR systems spatially distributed and two cooperative targets. The proposed fusion strategy consists of two steps: firstly a multi-temporal 3D target point-like model at each node of the radar network is created by joining together 3D target reconstructions taken at different time intervals, secondly, the multi-temporal 3D target point-like models, are combined so as to exploit spatial diversity of the multistatic system. The final results are then compared with the target CAD model to compare the estimated 3D cloud of points with the actual shape of the target.

The remainder of the paper is organized as follows. Section II briefly recalls the fundamentals of 3D InISAR imaging. Section III summarizes the fusion strategy. Section IV shows the results achieved with two different datasets. Finally, Section V is dedicated to remarks and conclusions.

II. 3D InISAR Imaging

A. Geometry

Consider the system geometry in Fig. 1 showing a monostatic interferometric setup. The L-shaped array is composed of three receivers AV, AC, AH lying onto a vertical and a horizontal baseline at distance d_V and d_H respectively in the reference system $T_{\xi'}$, which is embedded in the radar system. AC is also the transmitting antenna and is located at the antenna array phase center, that is at $\left(\xi_1^{'}=0, \xi_2^{'}=0, \xi_3^{'}=0\right)$.

The axis $\xi_2^{'}$ is chosen to be aligned with the radar line of sight (LoS) and the term $R_0(t)$ denotes the time varying distance between the radar and the reference point on the target. The rotational motion of the target is described by the angular rotation vector $\boldsymbol{\Omega_T}(t)$. The projection of $\boldsymbol{\Omega_T}(t)$ onto the plane orthogonal to the radar LoS (ξ_1, ξ_3) defines the effective rotation vector $\boldsymbol{\Omega_{eff}}(t)$, which contributes to the ISAR image formation. Let us define the time varying reference system T_x embedded in the target, centred on the target focusing point O and coincident with T_y at $t = 0$. As demonstrated in [10], the plane orthogonal to $\boldsymbol{\Omega_{eff}}(t)$ is the imaging plane. In this specific radar-target geometry, the x_3-axis is defined to be aligned with the effective rotation vector $\boldsymbol{\Omega_{eff}}(t)$, so that the image plane is identified as the (x_1, x_2) plane. The angle ϕ is the angle between the axes x_3 and ξ_3 and univocally identifies the direction of the effective rotation vector. In fact, the target motions cause $\boldsymbol{\Omega_{eff}}(t)$ to be rotated of ϕ along the LoS with respect to the vertical axis.

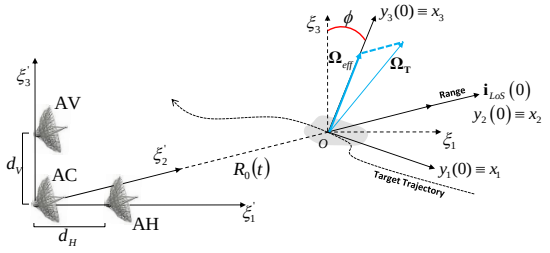

Fig. 1: Monostatic 3D InISAR system geometry.

B. Signal Modelling

The standard ISAR image formation processing consists of coherently processing the echo signal from a moving target at different aspect angles. Typically, the target is assumed to be a rigid body composed of independent point-like scatterers. Under this hypothesis, the received signal can be considered as the sum of independent echoes backscattered from each scattering centre and the target reflectivity function can be interpreted as the superposition of δ-like functions. Consequently, the ISAR image will result in a superposition of sinc-like functions centred at the scatterers coordinates in the image plane. Usually in ISAR signal processing the received signal is represented in a time (t)-frequency (f) format as this is a typical non-stationary signal. Hence, the multichannel received signal for a single ideal point scatterer in free space conditions and after motion compensation can be expressed as follows [11]:

$$S_R^{(i)}(f,t) = \rho \exp\left\{-j\frac{4\pi f}{c}\left[\mathbf{P}_y(t)\cdot \mathbf{i}_{LOS_y}^{(i)}(t)\right]\right\} W(f,t) \tag{1}$$

where c is the speed of light and ρ represents the reflectivity function, which describes the backscattering properties of the target. When the radar-target distance is significantly larger than the system's baselines, the aspect angle variation due to the spatial displacement between the receiving antennas can be considered negligible when compared to the aspect angle variation due to the target motion. Consequently, the scatterers can be supposed isotropic for all the channels and the reflectivity functions for each channel can be considered to have the same value, i.e. $\rho^{(i)} = \rho$. This condition is equivalent to the concept of spatial decorrelation for arrays. The term $\mathbf{P}_y = [y_1, y_2, y_3]$ denotes the position of a generic scatterer in T_y and $\mathbf{i}_{LOS_y}^{(i)}(t)$ is the LoS unit vector. The scalar product between these two terms represents the distance between the focusing point O and the projection of the considered scatterer onto the LOS. The window $W(f,t)$ is related to the system's Point Spread Function. It circumscribes the domain where the 2D Fourier transform (2D-FT) of the reflectivity function is defined and can be expressed as follows:

$$W(f,t) = \text{rect}\left[\frac{t}{T_{obs}}\right]\cdot \text{rect}\left[\frac{f-f_0}{B}\right] \tag{2}$$

where the function $rect(x)$ is equal to 1 for $|x| < 0.5$, 0 otherwise, T_{obs} is the observation time, f_0 is the carrier frequency and B is the transmitted signal bandwidth. A common method to form an ISAR image from the compensated data is the Range-Doppler (RD) approach [12] [13] [11]. This technique can be applied under two main assumptions:

1) Small variation of the total aspect angle
2) Sufficiently constant rotation vector

These assumptions are valid when considering a small observation time T_{obs}. In this case, the ISAR image can be obtained by applying a two-dimensional Fourier transform (2D-FT) to the focused received signal. As a result, the analytical form of the complex ISAR image of the i^{th} channel in the delay-time (τ) and Doppler (ν) domain can be expressed as [14]:

$$\begin{aligned} I^{(i)}(\tau,\nu) &= RD_{\substack{f\to\tau\\ t\to\nu}}\left\{S_R^{(i)}(f,t)\right\} = BT_{obs}\rho e^{j2\pi f_0\left(\tau-\frac{2}{c}K_0^{(i)}\right)} \\ &\times \text{sinc}\left[T_{obs}\left(\nu+\frac{2f_0}{c}K_1^{(i)}\right)\right]\text{sinc}\left[B\left(\tau-\frac{2}{c}K_0^{(i)}\right)\right] \end{aligned} \tag{3}$$

where $\text{sinc}(x) = \frac{\sin(\pi x)}{\pi x}$ and $RD_{\substack{f\to\tau\\ t\to\nu}}\{\cdot\}$ denotes the image formation process by means of the Range-Doppler technique.

The terms $K_0^{(i)}$ and $K_1^{(i)}$ are expressed for each channel as follows:

$$\begin{aligned} K_0^{AC} &\triangleq x_2 \\ K_1^{AC} &\triangleq c_2 \\ K_0^{AV} &\triangleq x_2 - \frac{d_V}{R_0}(x_1\sin\phi + x_3\cos\phi) \\ K_1^{AV} &\triangleq c_2 - \frac{d_V}{R_0}(c_1\sin\phi + c_3\cos\phi) \\ K_0^{AH} &\triangleq x_2 + \frac{d_H}{R_0}(x_3\sin\phi - x_1\cos\phi) \\ K_1^{AH} &\triangleq c_2 + \frac{d_H}{R_0}(c_3\sin\phi - c_1\cos\phi) \end{aligned} \tag{4}$$

where $\boldsymbol{x} = [x_1, x_2, x_3]$ is the vector of the scatterer coordinates with respect to the image plane while $\boldsymbol{c} = [c_1, c_2, c_3]$ results by expressing the term $\left[\mathbf{P}_y(t)\cdot \mathbf{i}_{LOS_y}^{(i)}(t)\right]$ in a closed form by solving the differential equation system $\dot{\mathbf{P}}_y(t) = \boldsymbol{\Omega_T}\times\mathbf{P}_y(t)$, with initial condition $\mathbf{P}_y(0) = \mathbf{P}_x$, that describes the target angular motions. For more details, the reader may refer to [15] [16] [6] [17]. As shown in Fig. 1, the term $R_0(t)$

denotes the distance between the radar in its phase centre and the target in the focusing point O. Here, it can be assumed $R_0(t) = R_0(0) = R_0$ due to the small observation time and the large radar-target distance.

C. 3D Image Formation

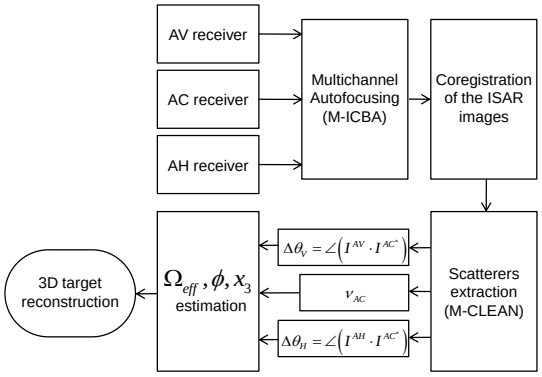

Fig. 2: 3D InISAR overall flowchart.

The overall flowchart of the 3D InISAR algorithm is depicted in Fig. 2.

First, the received signal is processed in each channel to obtain a 2D ISAR image for each receiver. All three 2D ISAR images are formed by applying the Range-Doppler technique. It can be reliably supposed that the target's 3D reflectivity function is projected onto the same image projection plane for all three images as the baseline lengths are much smaller than the radar-target distance. Then, it is possible to apply the multi-channel autofocus technique which is based on the ICBA [18] [19] [11]. The autofocus processing consists of removing the phase term produced by the target radial motion from the received signal. Due to the considered radar-target geometry, it is acceptable to assume that the distortions in all the three ISAR images are caused by the same phase term. Then, the focusing parameters are estimated for the central channel and applied to all ISAR images formed at the three receivers. Subsequently, the 2D images are coregistered and the main scatterers are extracted by means of the MC-CLEAN technique [20] [6]. The output of the MC-CLEAN technique is the range-Doppler position of each extracted scatterer and their complex amplitude.

Three main pieces of information are inferred from the received data for each scatterer:

- The phase difference $\Delta\theta_V$ at the peak of the $sinc$ functions in Equation (3) between the ISAR images of the vertical and central channels.
- The phase difference $\Delta\theta_H$ at the peak of the $sinc$ functions in Equation (3) between the ISAR images of the horizontal and central channels.
- The Doppler frequency of the central channel ν_{AC} extracted from the ISAR image.

These parameters are used to jointly estimate the amplitude of the effective rotation vector Ω_{eff} and its direction ϕ, which are linked to the scatterers height x_3 as follows:

$$x_3 = \frac{c}{4\pi f_0} R_0 \left(\frac{\triangle\theta_V}{d_V} \cos\phi - \frac{\triangle\theta_H}{d_H} \sin\phi \right) \tag{5}$$

In fact, the Doppler frequency of the central channel can be expressed by means of the following equation:

$$\nu_{AC} = -\frac{R_0 \Delta\theta_H}{2\pi d_H} \Omega_{eff} \cos\phi - \frac{R_0 \Delta\theta_V}{2\pi d_V} \Omega_{eff} \sin\phi \tag{6}$$

For a generic k^{th} scatterer, Equation (6) can be re-written as:

$$\nu_{ACk} = aA_k + bB_k \tag{7}$$

where $A_k \triangleq -\frac{R_0}{2\pi d_H}\Delta\theta_{H_k}$, $B_k \triangleq -\frac{R_0}{2\pi d_{V_k}}\Delta\theta_{V_k}$, $a \triangleq \Omega_{eff}\cos\phi$ and $b \triangleq \Omega_{eff}\sin\phi$.

The terms A_k, B_k and ν_{ACk} are directly estimated by processing the received signal. It can be noticed that Equation 7 represents the equation of a plane. The terms a and b can be estimated by means of a least square error as follows:

$$\tilde{a}, \tilde{b} = \min_{a,b} \sum_{k=1}^{M} \left[\nu_{ACk} - (aA_k + bB_k)\right]^2 \tag{8}$$

Finally, Ω_{eff} and ϕ can be jointly calculated through the estimates $\tilde{a}$ and $\tilde{b}$ as follows:

$$\begin{aligned} \hat{\Omega}_{eff} &= \sqrt{\tilde{a}^2 + \tilde{b}^2} \\ \hat{\phi} &= arctan\left(\frac{\tilde{b}}{\tilde{a}}\right) \end{aligned} \tag{9}$$

III. Multi-view 3D InISAR Image Fusion

As described in the previous sections, the height of each scatterer with respect to the image plane is obtained by jointly estimating the effective rotation vector Ω_{eff} and the rotation angle ϕ. In this way, the target's shape is reconstructed as a cloud of points in a 3D space. However, the correct positioning of these scatterers is linked to both the SNR and the phase coherence related to each of them. In other words, feeble scatterers may experience a low coherence and therefore being subject to estimation errors and consequently incorrect positioning. Typically, these two factors reduce the number of scattering centres that can be taken into account for 3D processing. As a consequence, this limits also the information that is needed to estimate the target's shape and size. In addition, shadowing effects may hide significant target features from the radar. An efficient way to increase the information about the target is to incoherently add a number of 3D reconstructions, which is the purpose of the 3D fusion algorithm described below. The great advantage of this method is that a 3D target reconstruction can be collected either at different acquisition times or from a generic number of spatially distributed interferometric sensors and then merged independently. Fig. 3 describes the flowchart of the 3D fusion algorithm.

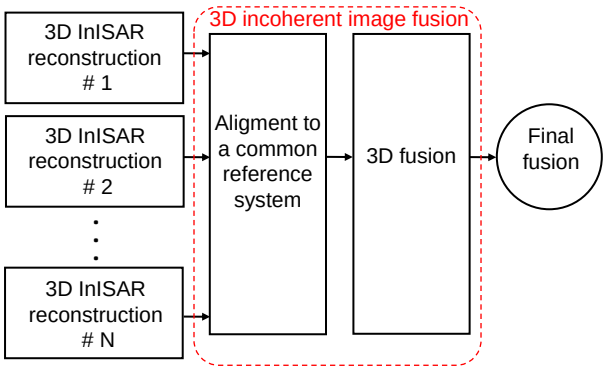

Fig. 3: High level 3D fusion flowchart.

This is of great interest for ATR/ATC systems as every single 3D fusion can add important information about the target with respect to a single reconstruction. Moreover, new information about the target of interest can be uploaded, when available, in order to update recognition and classification databases based on 3D InISAR imaging systems. More specifically, the 3D fusion algorithm can handle:

- Multi-temporal data: batches of received data selected at different times. This is a cost-effective solution, as information about the target can be added by using a single interferometric system.
- Multi-perspective data: data gathered by sensors deployed in spatially diverse positions. This method allows to obtain a 3D fusion that is a collection of 3D reconstructions obtained at different aspect angles. This may reduce or completely solve the shadowing problem.
- A combination of Multi-temporal and multi-prospective data.
- 3D InISAR fusions: 3D clouds of points that are already obtained by fusing 3D ISAR images.

A. 3D Fusion

The first step is to align the 3D reconstructions with respect to a common reference system. This is a necessary stage as each 3D image is formed by estimating the three spatial coordinates of each scatterer with respect to a given image plane, which is generally not the same for all the radar nodes. In order to accomplish this pre-alignment step, first, each 3D reconstruction is expressed according to its specific radar reference system by rotating the cloud of points by the estimated rotation angle $\hat{\phi}$. Then, supposing that the positions of the nodes of the net are known, it is possible to rotate all the reconstructions with respect to a fixed reference system. However, the 3D image formed at each sensor can be affected by shadowing effects and inaccurate estimation of ϕ. These effects can cause misalignments and for this reason it is necessary to perform a further alignment, which is another important step of the 3D fusion algorithm.

The 3D image fusion algorithm [21] works iteratively between pairs of 3D reconstructions and is structured in the following steps. Among the two 3D reconstructions of interest, let us identify one 3D image as the reference, composed of N scatterers. The other 3D image is composed of M scatterers.

- The height error is computed between the n^{th} scatterer of the reference and all the M scatterers of the other reconstruction in order to identify possible matches. The height error is defined as:

$$\epsilon_{nm} = |h_n - h_m| \tag{10}$$

- The height error is compared to a threshold Λ. A match $m_k(n)$ for the n^{th} scatterer is confirmed when the height error is lower than the threshold, where $k = 1..K_n$ and K_n is the number of matches for the specific scatterer of the reference.
- The reference and the other reconstruction are aligned by overlapping the match to the n_{th} scatterer, for all the matches.
- The euclidean distance is used to compute the number of scatterers that the two 3D images have in common in this particular position, denoted as $cs_k(n)$. A mean matching distance is also calculated as a reliability indicator and is expressed as follows:

$$mmd_k\,(n) = \frac{1}{C}\sum_{i=1}^{C} d_i\,(k) \tag{11}$$

  where C is the number of common scatterers and $d_i\,(k)$ is the i^{th} euclidean distance between the associated scatterers.
- For that particular n^{th} scatterer of the reference, among all the alignments obtained by overlapping each of the possible matches to the considered scatterer, the best alignment is selected based on the maximum number of common scatterers $cs_k(n)$ and the minimum mean matching distance $mmd_k\,(n)$.

These operations are repeated for all the N scatterers and the best final alignment is chosen between the best alignments of each scatterer based on the maximum number of common scatterers and the minimum mean matching distance. The block diagram of the 3D fusion algorithm is detailed in Fig. 4.

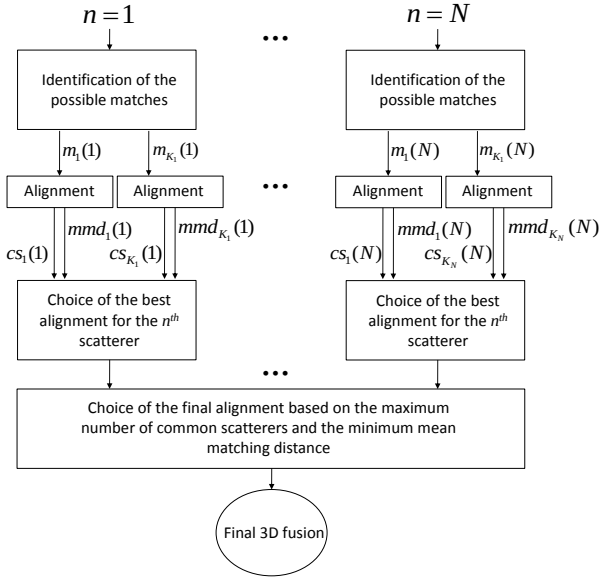

Fig. 4: 3D fusion block diagram.

It is important to underline that the necessary condition for the 3D fusion algorithm to achieve plausible results is that the incoming 3D reconstructions must have at least one scatterer in common. In addition, it can be noticed that the exhaustive search of the best alignment is performed for each of the N scattereres of the reference. Then, it is important to choose as the reference the 3D reconstruction composed of the smallest number of scatterers, that is $N < M$, in order to reduce the computational costs.

To summarize, the overall processing chain is shown in Fig. 5.

IV. Application of Multi-view 3D InISAR Image Fusion to Real Data

The multi-view 3D InISAR image fusion technique is applied to real data. In particular, the data was acquired during

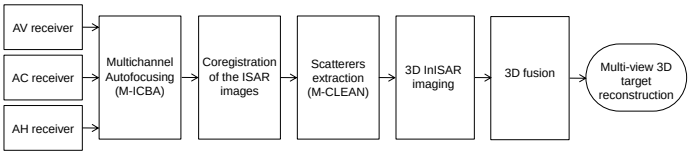

Fig. 5: Overall processing chain.

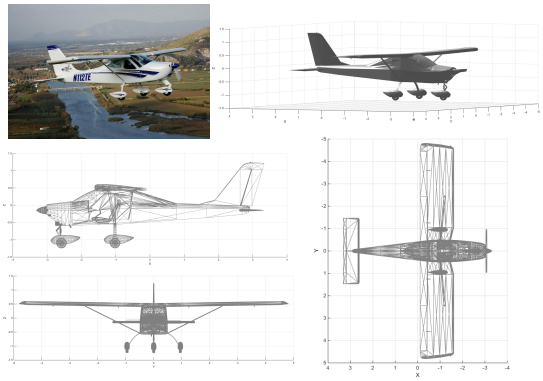

Fig. 6: Tecnam P92.

the NATO Set 196 joint trials on "Multichannel/Multistatic Radar Imaging of Non-cooperative Targets". Three ground-based 3D In-ISAR systems were used to acquire a echo of two targets, that were equipped with GPS/IMU (Global Positioning System/Inertial Measurement Unit) systems to measure their position and velocity. The first target is an Italian high-winged, light aircraft, built by Tecnam and named Tecnam P92. A picture of this aircraft and its relative CAD are shown in Fig. 6. The dimensions of the P92 aircraft are detailed in Tab. 1 and shown in Fig. 7.

Length	$6.6\ m$
Wingspan	$8.7\ m$
Horizontal stabilizer	$2.9\ m$
Height	$2.5\ m$

Tab. 1: Size of Tecnam P92

The second target is a training ship of the Italian Navy, named Astice. Astice and its relative CAD are shown in Fig. 8, while Astice's dimensions are detailed in Tab. 2.

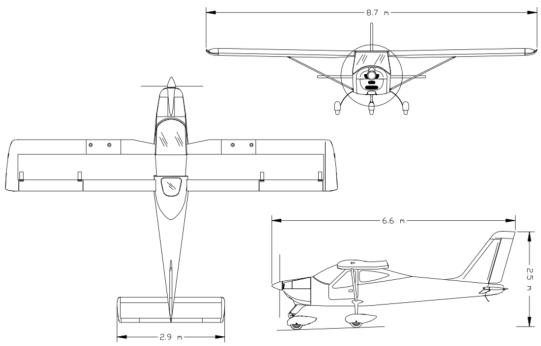

Fig. 7: Tecnam P92 [22].

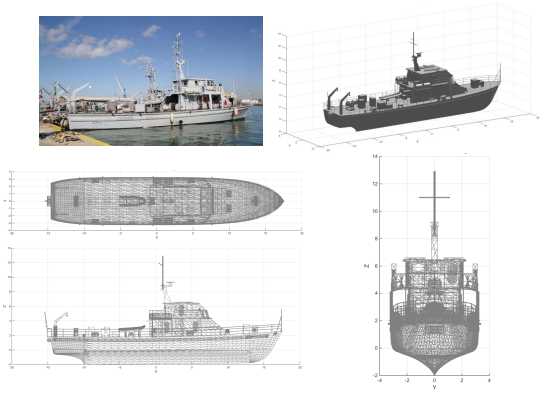

Fig. 8: Training ship Astice.

Length	$32.4\ m$
Width	$6.47\ m$
Deckhouse height	$\simeq 4.5\ m$
Main mast height	$\simeq 8\ m$

Tab. 2: Size of Astice

A. Scenarios Definition

The NATO Set 196 joint trials consisted of a 5-day measurement campaign which took place in Livorno from September 29 to October 3, 2014. The aim of SET-196 RTG and specifically of these trials was to explore the impact of multichannel/multistatic radar systems on 2D/3D imaging. In particular, improvements related to image features and their use for Automatic Target Recognition (ATR) systems were explored. Numerous research teams from eight nations took part in the trials and ten radar systems were used to simultaneously acquire data of a number of maritime and air targets [23] [24]. For the purpose of testing the described algorithm, the ground based radars HABRA1, HABRA2 and PIRAD were deployed. The two HABRA interferometric sensors are a Metasensing BV manufacture while the PIRAD prototype has borne from a collaboration between the Department of Information Engineering, University of Pisa, and the RaSS (Radar and Surveillance System) national laboratory. Both the HABRA and the PIRAD systems are Frequency Modulated Continuous Wave (FMCW) interferometric radars. Each of their antenna system consists of a transmitting element and three receivers arranged in an L-shape but spaced differently according to the system characteristics. The beampatterns of the antennas have a beam width of $60°$ along the azimuth direction and of $20°$ along the elevation. The PIRAD system is horizontally polarized and makes use of an X-band Fabry-Perot resonator while the HABRA system is vertically polarized and uses a microstrip patch flat panel antenna. Finally, a GPS PPS and a reference clock at 10 MHz of the GPS-DO system were installed on board the radars in order to reach time and phase synchronization between the systems. The main parameters of the HABRA and PIRAD systems are detailed in Fig. 9 and Fig. 10 respectively.

Two scenarios are presented in this paper in order to analyse the 3D InISAR multistatic fusion algorithm with a variety of targets.

Description	Value
Waveform	FMCW
Transmitted Frequency (X-band)	9,6 GHz
Band	300 MHz
Antenna Elevation beamwidth (-3dB)	20°
Antenna Azimuth beamwidth (-3dB)	60°
Transmitted power	Up to 37 dBm (34 dBm)
Polarization	V
PRF	1.22 KHz
Vertical/Horizontal Baseline	0.54/0.35 m

Fig. 9: HABRA Main parameters.

Description	Value
Waveform	FMCW
Transmitted Frequency (X-band)	10,7 GHz
Band	300 MHz
Antenna Elevation beamwidth (-3dB)	20°
Antenna Azimuth beamwidth (-3dB)	60°
Transmitted power	Up to 33 dBm (33 dBm)
Polarization	H
PRF	500 Hz
Vertical/Horizontal Baseline	0.47/0.41 m

Fig. 10: PIRAD main parameters.

The first scenario is depicted in Fig. 11. The data were collected on September 30, 2014, during the second day of trials. The Tecnam P92 aircraft was flying across the illuminating area at a height of about $76m$. The trajectory of the Tecnam P92 is highlighted in red and the locations of the three interferometric sensors HABRA1, HABRA2 and PIRAD are also shown. The position of the aircraft during the selected time intervals is pointed by the green arrow.

The second scenario is depicted in Fig. 12. The data were collected on October 3, 2014. The training ship Astice was navigating across the illuminated area with a number of non-cooperative targets. The trajectory of the cooperative target Astice is highlighted in red and, again, both the location of the three interferometric sensors and the position of Astice at the considered time intervals are shown.

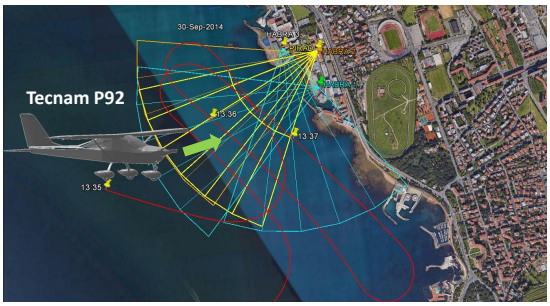

Fig. 11: Measurements set up - Tecnam P92.

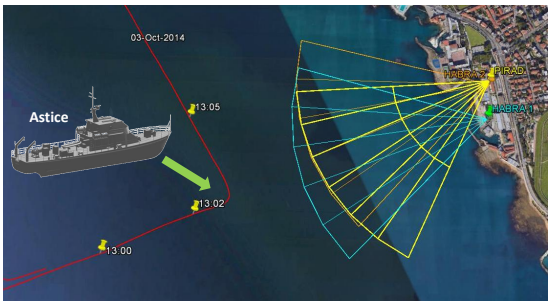

Fig. 12: Measurements set up - Astice.

B. *Application of Multi-view 3D*

1) Multi-temporal: The output of the 3D InISAR processing is a cloud of points located in a 3D space according to their range, cross-range and height coordinates estimation. This set of data points is intended to represent the target's shape and has a population density that depends on the number of extracted scatterers. Reliable monostatic 3D reconstructions are typically composed of a small number of scatterers for several reasons:

- Variations of SNR.
  The correct positioning of the extracted scattering centres is affected by the SNR associated to each of them. Then, reliable point clouds are often sparsely populated.
- Shadowing effects.
  Parts of the illuminated object might be covered depending on the specific radar-target geometry. This limits the amount of scatterers that can be extracted and then located in the 3D space.
- Geometrically adverse cases.
  2D ISAR images with little or no Doppler extension might be generated from received data corresponding to specific target's dynamics [25] [12] [11]. In this case, the standard range-Doppler image formation processing practically produces 1D ISAR images instead of 2D images and no scatterers can be extracted.

As a consequence, monostatic reconstructions might not carry enough information about the target for it to be identified or even for its overall dimensions to be estimated. For this reason, the whole received data set can be processed at different time intervals in order to obtain a multi-temporal data set within a single acquisition, as depicted in Fig. 13. In fact, sequences of 3D images typically show different scatterers from each other as a result of scintillation effects. Multiple images can

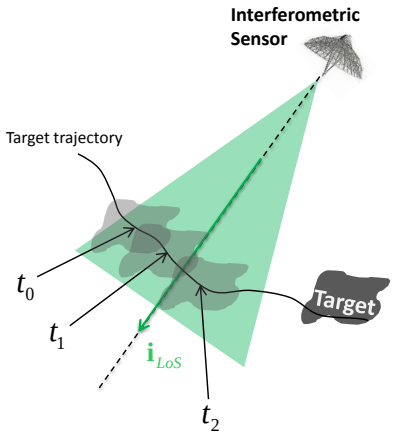

Fig. 13: Example of multi-temporal configuration.

be obtained at a single sensor and then joined together with the 3D fusion algorithm. Each of the reconstructions adds information to the final image, which will result more detailed and consequently will enable an improving understanding of the target's shape and size with respect to the monostatic case.

Multi-temporal results shown hereinafter refer to the aicraft Tecnam P92 and the training ship Astice when illuminated by the interferometric sensor HABRA 2.

a) Tecnam P92: The described multi-temporal data were collected on September 30, 2014. Three time intervals have been chosen within the total acquisition time in order to process different portions of the same data-set and consequently to exploit this combination of results to improve 3D target reconstruction. Details about the three batches of data are specified in Tab. 3.

	Acquisition time $[hh:mm:ss]$	T_{obs}
t_0	$13:36:47$	$1.1\ s$
t_1	$13:36:48$	$1\ s$
t_2	$13:36:49$	$1.1\ s$

Tab. 3: Selected time intervals - September 30, 2014 - Tecnam P92.

The observation time T_{obs} denotes the duration of each time interval. The range-Doppler maps of HABRA 2 corresponding to the three time intervals are shown in Fig. 14, where the target is enclosed in the red box.

Fig. 15 (a), (b) and (c) illustrate the 2D ISAR images at times t_0, t_1 and t_2 respectively, after autofocus and coregistration. The scatterers extracted by the MC-CLEAN technique are circled in black color.

After image autofocus and coregistration, the 3D InISAR image processing is applied to each batch of data. The height of each scatterer is estimated with respect to the image projection plane. Then, the output of the 3D InISAR processing before the prealignment step is the 3D image of the target rotated of the angle ϕ with respect to the radar reference system. The resulting 3D reconstructions pictured in the image plane reference system and obtained by processing the data at times t_0, t_1 and t_2 are depicted in Fig. 16, Fig. 17 and Fig. 18 respectively.

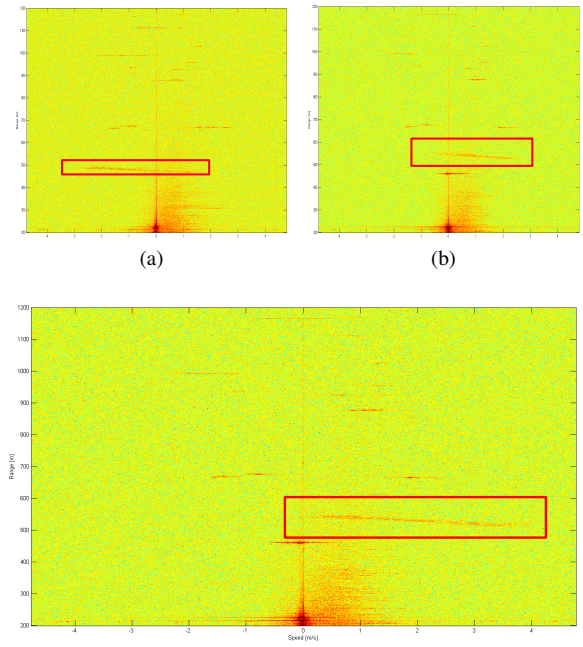

(a) (b)

(c)

Fig. 14: Range-Doppler maps of HABRA 2 at times (a) t_0 (b) $t_1 = t_0 + 1$ (c) $t_2 = t_0 + 2$. The aircraft Tecnam P92 is highlighted in the red box.

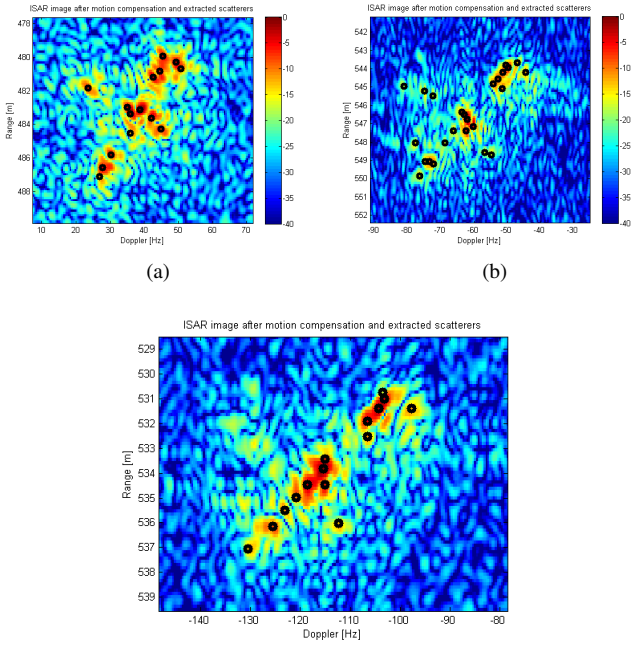

(a) (b)

(c)

Fig. 15: 2D ISAR images of the target collected at HABRA 2 at times (a) t_0 (b) $t_1 = t_0 + 1$ (c) $t_2 = t_0 + 2$. The black circles denotes the scatterers extracted by means of the MC-CLEAN technique - Tecnam P92.

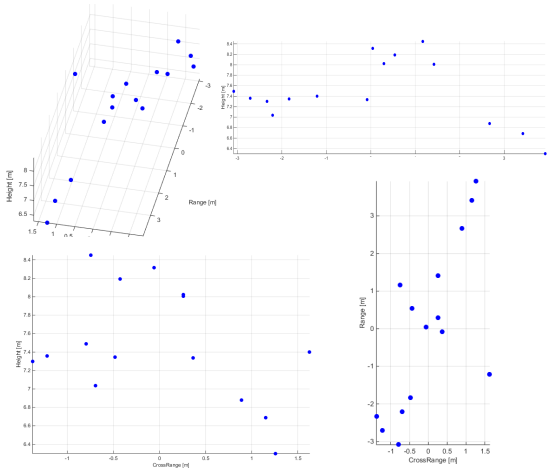

Fig. 16: InISAR 3D reconstruction relative to time t_0 - Tecnam P92.

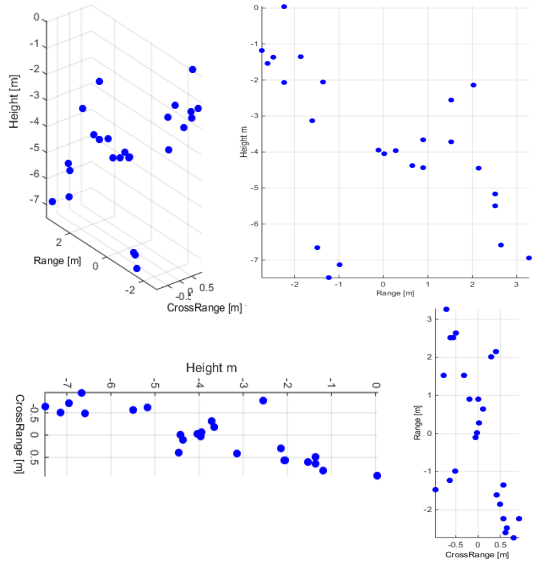

Fig. 17: InISAR 3D reconstruction relative to time $t_1 = t_0 + 1$ - Tecnam P92.

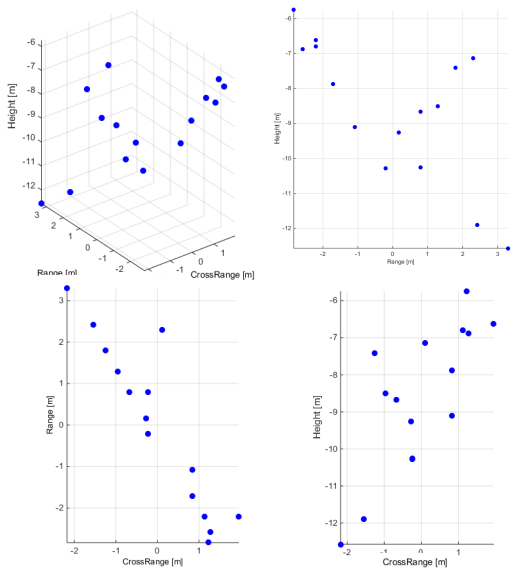

Fig. 18: InISAR 3D reconstruction relative to time $t_2 = t_0 + 2$ - Tecnam P92.

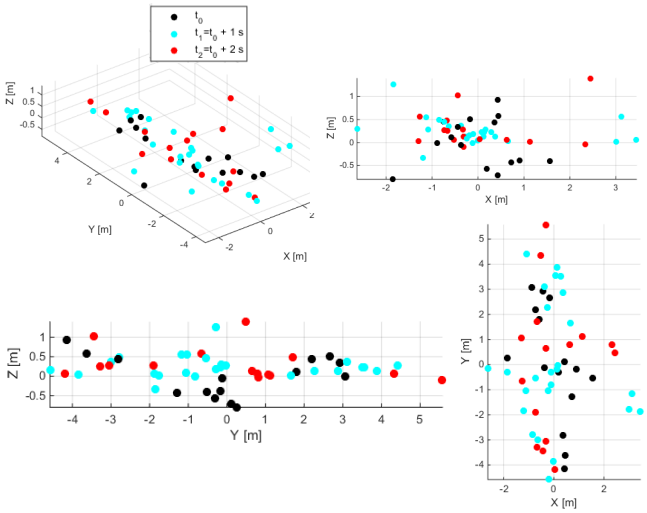

Fig. 19: Results of the prealignment step - multi-temporal data set - Tecnam P92.

It can be noticed that even at this point the interpretation of the 3D ISAR image is quite complex. This is true especially for relative small targets, as the aicraft P92, because the number of reliable scatterers that can be extracted from the 2D ISAR image is fairly small. In addition, the understanding of the target shape and size can be further reduced by shadowing effects. In fact, the particular radar-target geometry could cause regions of the target to be shielded from radar illumination and consequently the number of scatterers that can be located in the 3D space to be reduced. The estimation of the angle ϕ is then fundamental in order to rotate the reconstruction in the radar reference system. During the prealignment step, each 3D cloud of points is aligned with its centroid in the origin of a common reference system. It is worth noticing that the centroids of each 3D reconstruction depend on the specific part of the target that is imaged. Consequently, the coordinates of each centroid are not necessarily the same and this can cause misalignments, as shown in Fig. 19. It is interesting to mention that if the target trajectory and speed are such as to cause a rapid variation of the aspect angle, scintillation effects might reasonably result in very different 2D ISAR images even for contiguous time intervals. As a result, different scatterers might be more likely extracted and different parts of the target might be more likely imaged.

After applying the multi-view 3D InISAR image fusion , the resulting 3D final fusion is depicted in Fig. 20 and superimposed to the Tecnam P92 CAD in a $x-y-z$ reference system for a simpler visualization.

Tab. 4 shows the estimation of the main dimensions of the aircraft for the monostatic 3D reconstructions and for the final fusion in comparison to the real aircraft size.

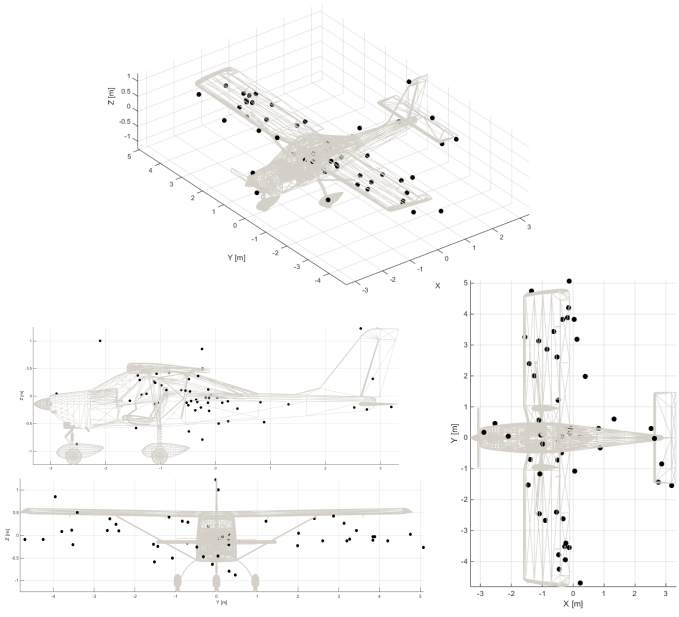

Fig. 20: Multi-temporal final fusion - Tecnam P92.

	Length	Wingspan	Horizontal stabilizer	Height
Actual size	$6.6[m]$	$8.7[m]$	$2.9[m]$	$2.5[m]$
t_0	$3.4[m]$	$7.2[m]$	$-[m]$	$1.7[m]$
t_1	$6[m]$	$8.9[m]$	$0.7[m]$	$1.6[m]$
t_2	$3.7[m]$	$9.7[m]$	$-[m]$	$1.5[m]$
Final fusion	$6.1[m]$	$9.7[m]$	$1.5[m]$	$2.1[m]$

Tab. 4: Estimated dimensions - Multitemporal case - Tecnam P92.

It is worth noting that 3D fusion strongly enhance the understanding of the target shape and size. The main structures of the aircraft as the wings, the body and the tail are easily recognizable and the overall dimensions of the Tecnam P92 are better estimated. From Tab. 4 can be deduced for example that the aircraft's tail is visible only in the monostatic 3D reconstruction at t_1. When combining all the three reconstructions, the tail of the aircraft can be easily spotted and it is evident that about half of the horizontal stabilizer is reconstructed, in accordance to the estimated dimensions.

b) Training ship Astice: The data shown in this section were collected on October 3, 2014. The training ship Astice was crossing the region illuminated by the interferometric sensor PIRAD along with other targets, as depicted in Fig. 21, where Astice is highlighted in the red box. The three range-Doppler maps corresponding to the different time intervals t_0, $t_1 = t_0 + 2$ and $t_2 = t_0 + 3$ are shown in Fig. 21. The selected time intervals are detailed in Tab. 5.

	Acquisition time $[hh:mm:ss]$	T_{obs}
t_0	$13:02:40$	$0.9\ s$
t_1	$13:02:42$	$0.9\ s$
t_2	$13:02:43$	$0.8\ s$

Tab. 5: Selected time intervals - October 3, 2014 - Astice.

As expected, the data processed at different time intervals produce different 2D ISAR images due to the target complex motion. Fig. 22 illustrates the 2D ISAR images of each time

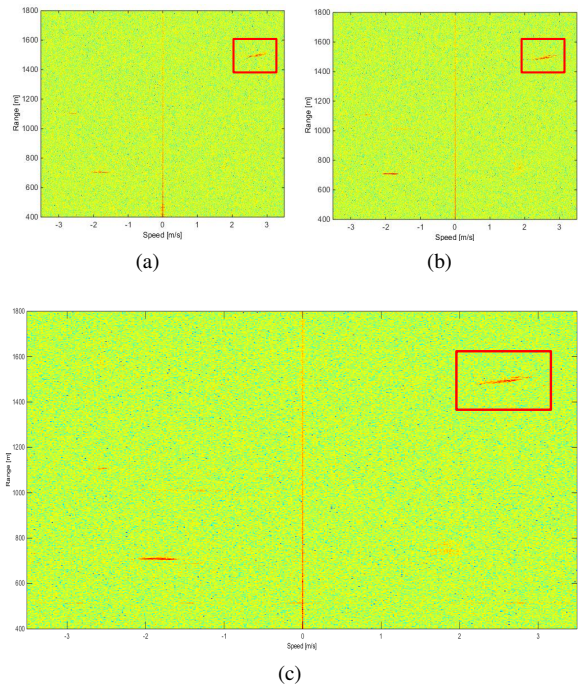

Fig. 21: Range-Doppler maps of PIRAD at times (a) t_0 (b) $t_1 = t_0 + 2$ (c) $t_2 = t_0 + 3$. The training ship Astice is highlighted in the red box.

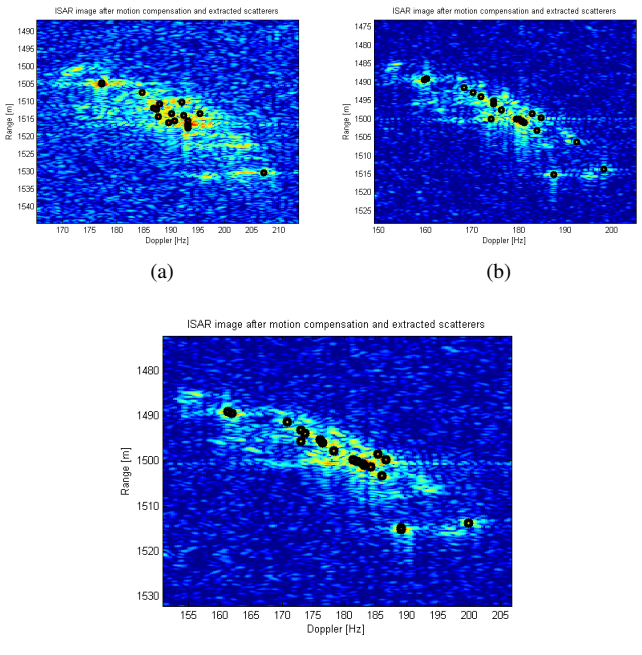

Fig. 22: 2D ISAR images of the target collected at PIRAD at times (a) t_0 (b) $t_1 = t_0 + 2$ (c) $t_2 = t_0 + 3$. The black circles denotes the scatterers extracted by means of the MC-CLEAN technique - Astice.

step and the scatterers extracted by means of the MC-CLEAN technique.

Figures 23-25 show the output of the 3D InISAR processing for the three time intervals before the prealignment stage.

The output of the prealignment block is depicted in Fig. 26, where the 3D images are rotated by the estimated rotation

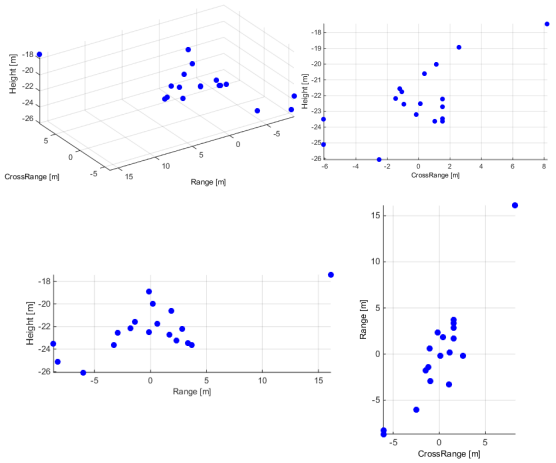

Fig. 23: InISAR 3D reconstruction relative to time t_0 - Astice.

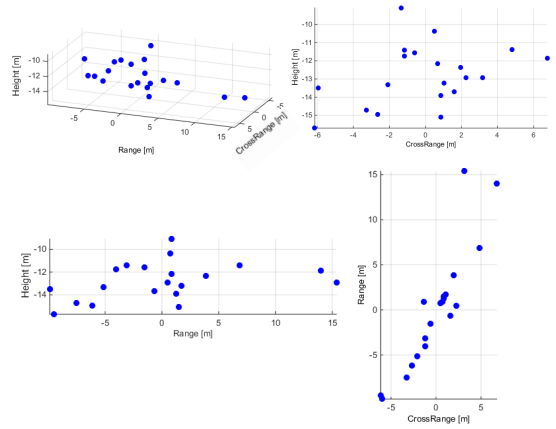

Fig. 24: InISAR 3D reconstruction relative to time $t_1 = t_0 + 2$ - Astice.

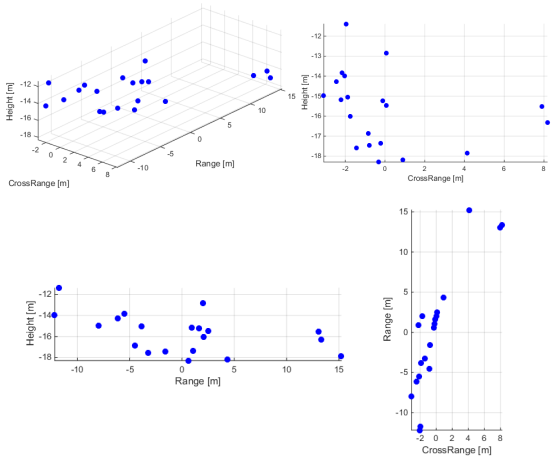

Fig. 25: InISAR 3D reconstruction relative to time $t_2 = t_0 + 3$ - Astice.

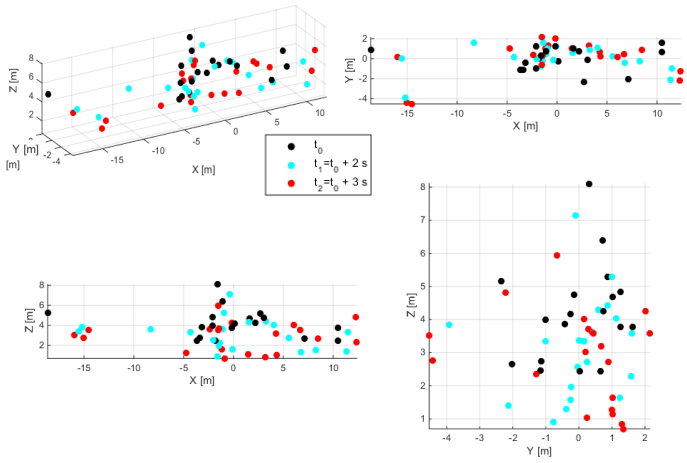

Fig. 26: Results of the prealignment step - multi-temporal data set - Astice.

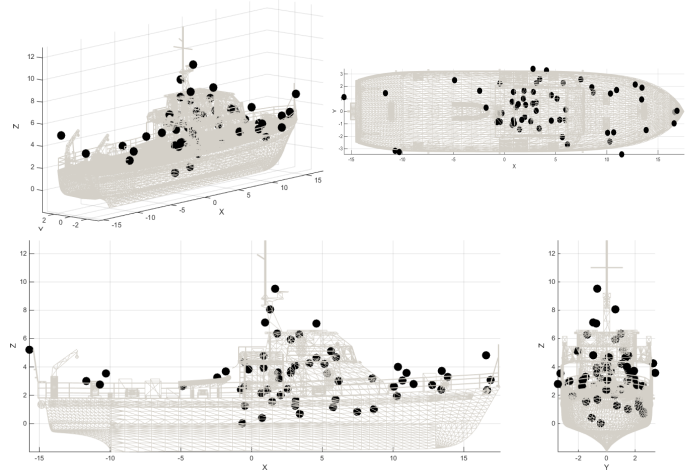

Fig. 27: Multi-temporal final fusion - Astice.

angle ϕ and located in a common reference system with their centroids in [0,0,0]. Again, shadowing effects and possible incorrect estimation of the rotation angle cause misalignments and the overall size of the ship cannot be inferred. The 3D fusion algorithm aligns the monostatic 3D reconstructions by exploiting the scatterers height and the Euclidean distance. The resulting final fusion is shown in Fig. 26, while Tab. 6 details the estimated target dimensions for the monostatic cases and for the multi-temporal fusion compared with the actual size of the training ship Astice.

	Length	Width	Height
Actual size	$32.4[m]$	$6.47[m]$	$12.5[m]$
t_0	$29.14[m]$	$3.96[m]$	$5.6[m]$
t_1	$21.77[m]$	$5.95[m]$	$9.5[m]$
t_2	$28.32[m]$	$6.67[m]$	$5.24[m]$
Final fusion	$32.5[m]$	$6.8[m]$	$9.5[m]$

Tab. 6: Estimated dimensions - Multitemporal case - Astice.

It is worth pointing out that the multi-temporal 3D reconstruction contains the joint information from the three time intervals and consequently it improves 3D target reconstruction. As an example, it can be noted that after the

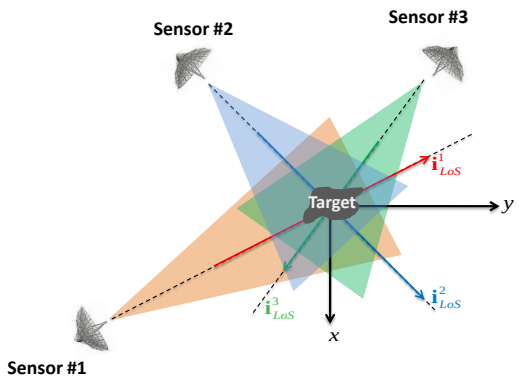

Fig. 28: Example of multistatic configuration.

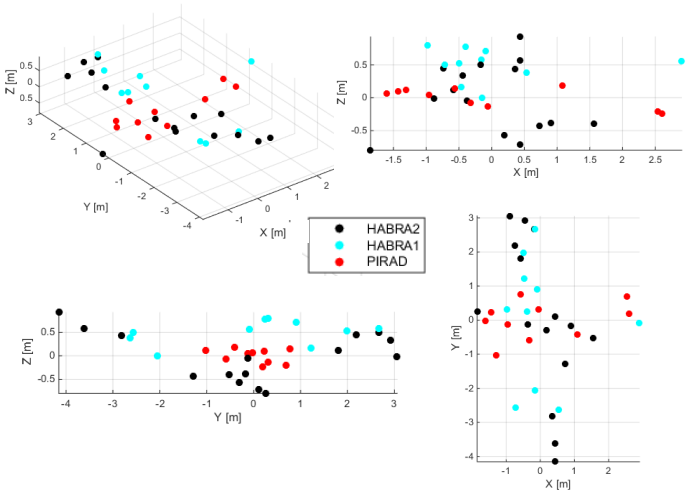

Fig. 29: Results of the prealignment step - multi-perspective data set - Tecnam P92.

multi-temporal fusion, the main structures of the ship as the bow, the deckhouse, the mast and the stern are more easily distinguishable with respect to the single monostatic cases. This is because, even if similar, each monostatic 3D reconstruction derives from the analysis of temporally diverse data batches and thus add information to a single acquisition.

2) Multistatic: As described above, temporal diversity at a single sensor can be exploited to obtain a final 3D image with the 3D fusion technique. The information contained in single 3D reconstructions, corresponding to different time intervals, is gathered in this final richer and more detailed 3D image. Although this is a cost-effective solution, some critical issues might limit improvements in the multi-temporal fusion.

First, particular radar-target geometries produce ISAR images with no Doppler extension, basically reducing a 2D ISAR image to a 1D ISAR image. As an example, a target that intentionally or accidentally follows a trajectory along the radar Line of Sight (LoS) with little or no oscillations (pitch and yaw). In this case, it is impossible to obtain a 3D reconstruction even if processing time-diverse batches of the received data. A second issue might arise if very similar 2D ISAR images, and consequently very similar 3D reconstructions, are obtained at the different time intervals. In this case, the final multi-temporal fusion adds very little information to the monostatic reconstructions. Last but not least, the shadowing effect is not reduced significantly as the target may show almost the same view to the radar.

Such limitations can be overcome by using a multistatic configuration, that is a network of spatially distributed imaging radars as depicted in Fig. 28.

This approach takes advantages from the spatial diversity, which exploits different aspect angles and consequently generate multi-perspective data sets.

Results of the multistatic processing that are shown here are related to sensors HABRA 1, HABRA 2 and PIRAD illuminating the aircraft Tecnam P92 on September 30, 2014 and the training ship Astice on October 3, 2014.

a) Tecnam P92: Tab. 7 gives details about the specific time interval chosen for each sensor.

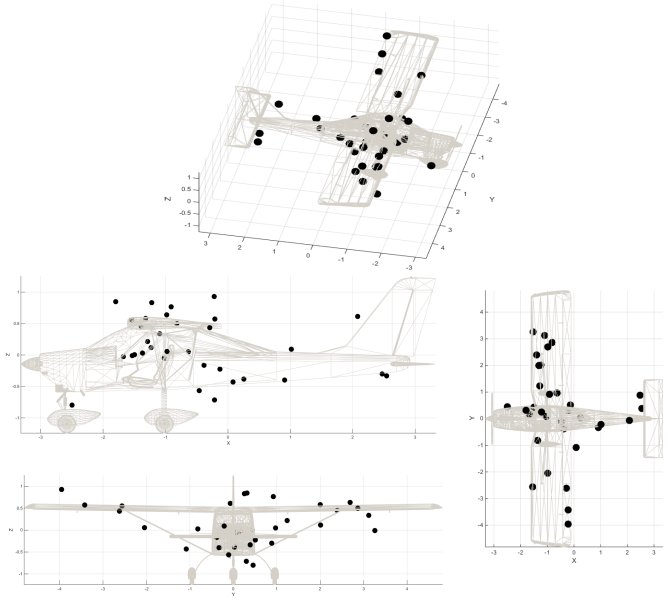

Fig. 30: Multistatic final fusion - Tecnam P92.

	Acquisition time $[hh:mm:ss]$	T_{obs}
HABRA 1	13 : 36 : 50	0.9 s
HABRA 2	13 : 36 : 47	1.1 s
PIRAD	13 : 36 : 41	0.9 s

Tab. 7: Selected sensors and time intervals - September 30, 2014 - Tecnam P92

Fig. 29 shows the three monostatic 3D reconstructions rotated by the estimated angle $\hat{\phi}$ with their centroids in the origin of a common reference system.

The multi-perspective 3D fusion is depicted in Fig. 30 while the estimated dimensions are listed in Tab. 8.

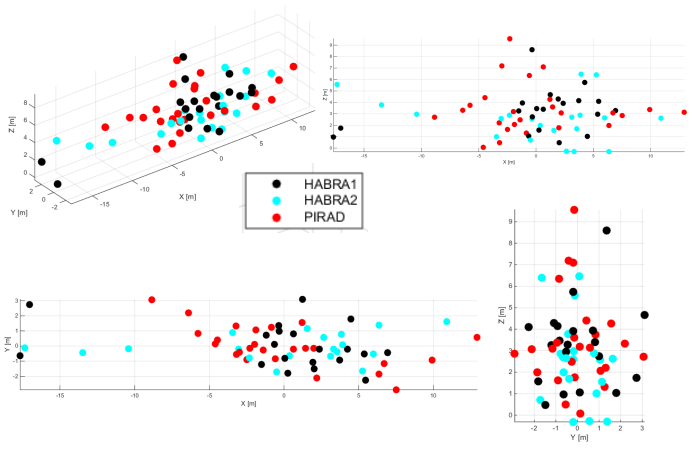

Fig. 31: Results of the prealignment step - multi-perspective data set - Astice.

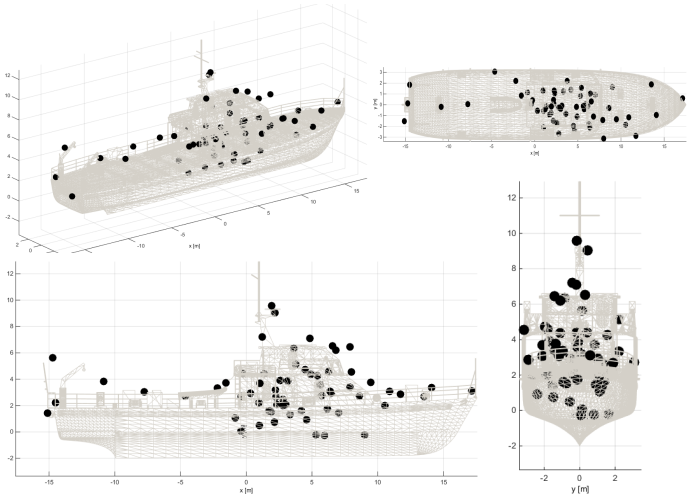

Fig. 32: Multistatic final fusion - Astice.

	Length	Wingspan	Horizontal stabilizer	Height
Actual size	$6.6[m]$	$8.7[m]$	$2.9[m]$	$2.5[m]$
HABRA 1	$3.8[m]$	$5.3[m]$	$-[m]$	$0.8[m]$
HABRA 2	$3.4[m]$	$7.2[m]$	$-[m]$	$1.7[m]$
PIRAD	$4.2[m]$	$1.8[m]$	$0.5[m]$	$0.4[m]$
Final fusion	$5[m]$	$7.2[m]$	$1[m]$	$1.7[m]$

Tab. 8: Estimated dimensions - Multistatic case - Tecnam P92

It can be noted by observing Fig. 29 that PIRAD is able to image only the body of the plane. Then, it would be impossible to identify the target or even classify it as an aircraft if only this 3D reconstruction was available. In addition, the 3D image obtained by HABRA 2 shows the wingspan but not the tail of the aircraft. Thus, the whole length of the target would not be estimated. When joining together all the 3D images, the shape of the target is easily recognizable and the target dimensions are estimated with higher precision.

b) Training ship Astice: Tab. 9 describes the selected sensors and the processed time intervals.

	Acquisition time $[hh:mm:ss]$	T_{obs}
HABRA 1	$13:02:38$	$0.9\ s$
HABRA 2	$13:02:38$	$0.9\ s$
PIRAD	$13:02:42$	$0.9\ s$

Tab. 9: Selected sensors and time intervals - October 3, 2014 - Astice

As a result of the prealignment processing, the 3D images are aligned as shown in Fig. 31.

The output of the 3D fusion algorithm is shown in Fig. 32, which illustrates the final 3D multistatic fusion obtained by incoherently fusing the three monostatic reconstructions obtained by HABRA 1, HABRA 2 and PIRAD.

Tab. 10 details the estimated ship dimensions for the monostatic cases and the multistatic fusion against the actual size.

	Length	Width	Height
Actual size	$32.4[m]$	$6.47[m]$	$12.5[m]$
HABRA 1	$24.6[m]$	$5.4[m]$	$8.1[m]$
HABRA 2	$28.3[m]$	$3.3[m]$	$6.8[m]$
PIRAD	$21.8[m]$	$6[m]$	$9.5[m]$
Final fusion	$32.2[m]$	$6.2[m]$	$9.8[m]$

Tab. 10: Estimated dimensions - Multistatic case - Astice

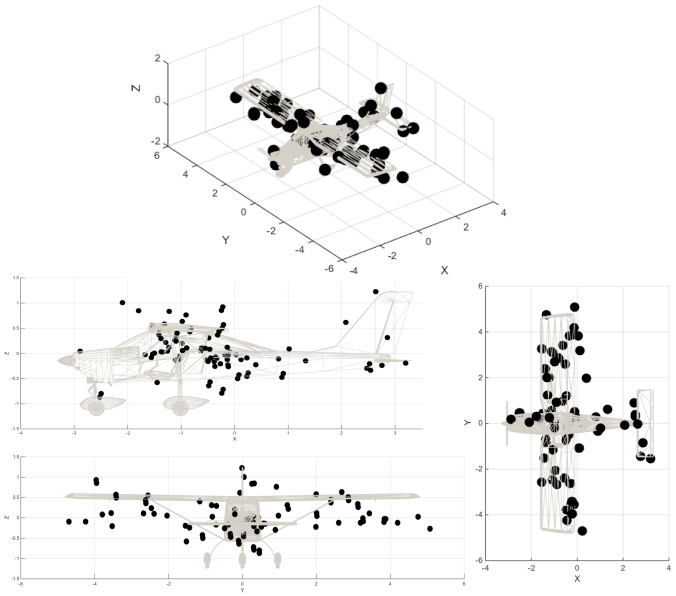

Fig. 33: Multi-view final fusion - Tecnam P92.

Also in this case, the final 3D cloud of points results more dense and the target's shape is reconstructed. In addition, the estimation of the target length, width and height are more accurate with respect to the monostatic cases.

3) Multi-temporal/Multistatic: Further information to the final image can be added by combining multi-temporal and multi-perspective data. The availability of both these configurations gives the opportunity to use a larger number of 3D reconstructions as input to the 3D fusion algorithm and consequently to obtain a more complete and more detailed 3D image of the target.

a) Tecnam P92: The multi-temporal and the multistatic reconstructions of the aircraft Tecnam P92 are fused by means of the 3D fusion algorithm in order to exploit both the space and time diversity of the received data. The resulting multi-view final fusion is shown in Fig. 33.

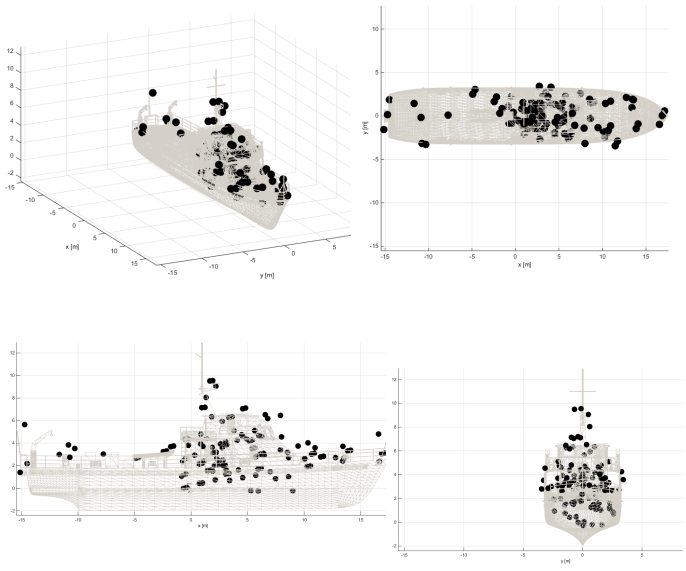

Fig. 34: Multi-view final fusion - Astice.

	Length	Wingspan	H. stabilizer	Height
Actual size	$6.6[m]$	$8.7[m]$	$2.9[m]$	$2.5[m]$
Multi-temporal final fusion	$6.1[m]$	$9.7[m]$	$1.5[m]$	$2.1[m]$
Multistatic final fusion	$5[m]$	$7.2[m]$	$1[m]$	$1.7[m]$
Multi-view final fusion	$6.1[m]$	$9.7[m]$	$2.4[m]$	$2.1[m]$

Tab. 11: Estimated dimensions - Multi-view case - Tecnam P92

It is worth noting that the multi-view 3D reconstruction best describe the target shape and size, which is very important for ATR/ATC systems, as observable in Tab. 11.

b) Training ship Astice: Also for the training ship Astice the multi-temporal and the multistatic data are used to form a final 3D reconstruction by means of the 3D fusion technique and is depicted in Fig. 34. Again, the cloud of points that are located in a 3D space is highly populated and best highlights the main structures of the target. Moreover, the multi-temporal/multistatic fusion accurately estimates the target dimensions, as detailed in Tab. 12.

	Length	Width	Height
Actual size	$32.4[m]$	$6.47[m]$	$12.5[m]$
Multi-temporal final fusion	$32.58[m]$	$6.84[m]$	$9.5[m]$
Multistatic final fusion	$32.2[m]$	$6.2[m]$	$9.8[m]$
Multi-view final fusion	$32.8[m]$	$6.8[m]$	$9.8[m]$

Tab. 12: Estimated dimensions - Multi-view case - Astice

V. Conclusions

In this paper, it has been shown that 3D image reconstruction using multiple views greatly enhances the system capability to reconstruct 3D non-cooperative target images effectively. The fusion of 3D point clouds obtained by using multiple temporal and multiple node acquisitions creates a more densely populated point cloud that better represents the target of interest and allows for important features to be extracted more accurately and reliably. Although the implementation of ATR systems that make use of 3D reconstructions is still not in place, the results shown here are a strong encouragement to use this new technology to strengthen radar image based ATR.

VI. Acknowledgement

The authors would like to thank the Centro di Supporto e Sperimentazione Navale - Istituto per le Telecomunicazioni e l'Elettronica "Giancarlo Vallauri" (CSSN-ITE), an experimental facility of the Italian Navy, for technical and logistic support given during the experiment that took place in Livorno. The authors would also to thanks the NATO for partially funding this work under the framework of The NATO Set 196 "Multichannel/Multistatic Radar Imaging of Non-cooperative Targets".

References

[1] X. Xu and R. Narayanan, "Three-dimensional interferometric ISAR imaging for target scattering diagnosis and modeling," *Image Processing, IEEE Transactions on*, vol. 10, pp. 1094 –1102, Jul 2001.

[2] J. A. Given and W. R. Schmidt, "Generalized isar - part i: an optimal method for imaging large naval vessels," *IEEE Transactions on Image Processing*, vol. 14, pp. 1783–1791, Nov 2005.

[3] J. A. Given and W. R. Schmidt, "Generalized isar-part ii: interferometric techniques for three-dimensional location of scatterers," *IEEE Transactions on Image Processing*, vol. 14, pp. 1792–1797, Nov 2005.

[4] C. Ma, T. S. Yeo, Q. Zhang, H. S. Tan, and J. Wang, "Three-dimensional isar imaging based on antenna array," *IEEE Transactions on Geoscience and Remote Sensing*, vol. 46, pp. 504–515, Feb 2008.

[5] G. Wang, X.-G. Xia, and V. C. Chen, "Three-dimensional isar imaging of maneuvering targets using three receivers," *IEEE Transactions on Image Processing*, vol. 10, pp. 436–447, Mar 2001.

[6] M. Martorella, D. Staglianò, F. Salvetti, and N. Battisti, "3d interferometric isar imaging of noncooperative targets," *IEEE Transactions on Aerospace and Electronic Systems*, vol. 50, pp. 3102–3114, October 2014.

[7] F. Salvetti, E. Giusti, D. Staglianò, and M. Martorella, "Incoherent fusion of 3d inisar images using multi-temporal and multi-static data," in *2016 IEEE Radar Conference (RadarConf)*, pp. 1–6, May 2016.

[8] S. Brisken and J. Ender, "Block-sparse 3-d isar image reconstruction in a non-coherent multistatic scenario," in *2015 IEEE Radar Conference (RadarCon)*, pp. 0265–0269, May 2015.

[9] P. van Dorp, M. P. G. Otten, and J. M. M. Verzeilberg, "Coherent multistatic isar imaging," in *IET International Conference on Radar Systems (Radar 2012)*, pp. 1–6, Oct 2012.

[10] J. Walker, "Range-Doppler Imaging of Rotating Objects," *Aerospace and Electronic Systems, IEEE Transactions on*, vol. AES-16, pp. 23 –52, Jan. 1980.

[11] M. Martorella, F. Berizzi, and B. Haywood, "Contrast maximisation based technique for 2-D ISAR autofocusing," *Radar, Sonar and Navigation, IEE Proceedings* -, vol. 152, pp. 253 – 262, Aug. 2005.

[12] D. Wehner, *High-Resolution Radar*. Artech House Radar Library, Artech House, 1995.

[13] F. Berizzi and M. Diani, "Target angular motion effects on ISAR imaging," *Radar, Sonar and Navigation, IEE Proceedings* -, vol. 144, no. 2, pp. 87–95, 1997.

[14] M. Martorella, "Introduction to inverse synthetic aperture radar," in *Elsevier Academic Press Library in Signal Processing: Communications and Radar Signal Processing*, (Vol. 2), 1st Ed., Sept 2013.

[15] F. Berizzi, E. Dalle Mese, M. Diani, and M. Martorella, "High-resolution ISAR imaging of maneuvering targets by means of the range instantaneous Doppler technique: modeling and performance analysis," *Image Processing, IEEE Transactions on*, vol. 10, pp. 1880 –1890, Dec 2001.

[16] A. Scaglione and S. Barbarossa, "Estimating motion parameters using parametric modeling based on time-frequency representations," in *Radar 97 (Conf. Publ. No. 449)*, pp. 280 –284, Oct 1997.

[17] M. Martorella, F. Salvetti, and D. Staglianò, "3d target reconstruction by means of 2d-isar imaging and interferometry," in *2013 IEEE Radar Conference (RadarCon13)*, pp. 1–6, April 2013.

[18] F. Berizzi, M. Martorella, B. Haywood, E. D. Mese, and S. Bruscoli, "A survey on isar autofocusing techniques," in *Image Processing, 2004. ICIP '04. 2004 International Conference on*, vol. 1, pp. 9–12 Vol. 1, Oct 2004.

[19] M. Martorella, F. Berizzi, and S. Bruscoli, "Use of Genetic Algorithms for Contrast and Entropy Optimization in ISAR Autofocusing," *EURASIP Journal on Advances in Signal Processing*, vol. 2006, no. 1, p. 087298, 2006.

[20] M. Martorella, D. Staglianò, F. Salvetti, and F. Berizzi, "3D interferometric ISAR," in *Radar Imaging for Maritime Observation* (F. Berizzi, M. Martorella, and E. Giusti, eds.), ch. 6, pp. 139–175, CRC Press, 2016.

[21] F. Salvetti, E. Giusti, D. Staglianò, and M. Martorella, "Multistatic 3d isar image reconstruction," in *2015 IEEE Radar Conference (RadarCon)*, pp. 0640–0645, May 2015.

[22] TECNAM, "Tecnam p92 eaglet us-lsa datasheet."

[23] F. Salvetti, E. Giusti, D. Staglianò, and M. Martorella, "Multistatic 3d inisar imaging," in *NATO SET-228 Specialists Meeting on Radar Imaging for Target Identification*, 2015.

[24] M. Martorella, D. Staglianò, S. Lischi, E. Giusti, F. Salvetti, A. B. S. Gelli, D. Cataldo, R. Massini, A. Lupidi, S. Brisken, A. Fontana, P. Berens, P. Krisic, M. Baczyk, M. Gashinova, M. Cherniakov, H.-T. Tran, D. Greig, A. Meta, L. Corucci, E. Kalender, and W. Nel, "Multistatic/multichannel radar imaging in practice: the nato set-196 trials," in *NATO SET-228 Specialists Meeting on Radar Imaging for Target Identification*, 2015.

[25] D. A. Ausherman, A. Kozma, J. L. Walker, H. M. Jones, and E. C. Poggio, "Developments in Radar Imaging," *Aerospace and Electronic Systems, IEEE Transactions on*, vol. AES-20, pp. 363 –400, July 1984.